

Article

# Weak Coordinating Character of Organosulfonates in Oriented Silica Films: An Efficient Approach for Immobilizing Cationic Metal-Transition Complexes

Samuel Ahoulou <sup>1,2</sup>, Clara Richart <sup>1</sup>, Cédric Carteret <sup>1</sup>, Sébastien Pillet <sup>2,\*</sup>, Neus Vilà <sup>1,\*</sup> and Alain Walcarius <sup>1,\*</sup> 

<sup>1</sup> LCPME, CNRS, Université de Lorraine, F-54000 Nancy, France

<sup>2</sup> CRM2, CNRS, Université de Lorraine, F-54000 Nancy, France

\* Correspondence: sebastien.pillet@univ-lorraine.fr (S.P.); neus.vila@univ-lorraine.fr (N.V.); alain.walcarius@univ-lorraine.fr (A.W.)

**Abstract:** Iron (II) tris(2,2'-bipyridine) complexes,  $[\text{Fe}(\text{bpy})_3]^{2+}$ , have been synthesized and immobilized in organosulfonate-functionalized nanostructured silica thin films taking advantage of the stabilization of  $[\text{Fe}(\text{H}_2\text{O})_6]^{2+}$  species by hydrogen bonds to the anionic sulfonate moieties grafted to the silica nanopores. In a first step, thiol-based silica films have been electrochemically generated on indium tin oxide (ITO) substrates by co-condensation of 3-mercaptopropyltrimethoxysilane (MPTMS) and tetraethoxysilane (TEOS). Secondly, the thiol function has been modified to sulfonate by chemical oxidation using hydrogen peroxide in acidic medium as an oxidizing agent. The immobilization of  $[\text{Fe}(\text{bpy})_3]^{2+}$  complexes has been performed in situ in two consecutive steps: (i) impregnation of the sulfonate functionalized silica films in an aqueous solution of iron (II) sulfate heptahydrate; (ii) dipping of the iron-containing mesostructures in a solution of bipyridine ligands in acetonitrile. The in situ formation of the  $[\text{Fe}(\text{bpy})_3]^{2+}$  complex is evidenced by its characteristic optical absorption spectrum, and elemental composition analysis using X-ray photoelectron spectroscopy. The measured optical and electrochemical properties of immobilized  $[\text{Fe}(\text{bpy})_3]^{2+}$  complexes are not altered by confinement in the nanostructured silica thin film.

**Keywords:** mesoporous silica films; polypyridyl metal complexes; confinement effects; metal ligand coordination; organic–inorganic hybrids; iron-bipyridine derivatives; modified electrodes



**Citation:** Ahoulou, S.; Richart, C.; Carteret, C.; Pillet, S.; Vilà, N.; Walcarius, A. Weak Coordinating Character of Organosulfonates in Oriented Silica Films: An Efficient Approach for Immobilizing Cationic Metal-Transition Complexes. *Molecules* **2022**, *27*, 5444. <https://doi.org/10.3390/molecules27175444>

Academic Editor: Haralampos N. Miras

Received: 21 July 2022

Accepted: 17 August 2022

Published: 25 August 2022

**Publisher's Note:** MDPI stays neutral with regard to jurisdictional claims in published maps and institutional affiliations.



**Copyright:** © 2022 by the authors. Licensee MDPI, Basel, Switzerland. This article is an open access article distributed under the terms and conditions of the Creative Commons Attribution (CC BY) license (<https://creativecommons.org/licenses/by/4.0/>).

## 1. Introduction

The ability of organosulfonate anions to coordinate transition metal centers remains quite unexplored since they are considered as poor ligands not able to displace solvent molecules from the first coordination sphere of a metal ion efficiently [1]. Examples with direct sulfonate-to-metal coordination are rarely described; they are often limited to representative elements or closed shell  $d^{10}$  cations (Ag(I) and Cd(II)) [2]. Even though, some examples of frameworks made of divalent transition metal imidazole complexes bearing 1,5-naphthalenedisulfonate have been already reported. They provide direct sulfonate–metal linkages constituting the first known compounds with open d-shell transition metal with octahedral coordination [3]. Weak interactions with metal ions that lead to the formation of robust solids assisted by hydrogen bonding have been also reported in the case of divalent and trivalent metals from the first-row transition metal [4]. In this sense, the ability of sulfonate moieties to interact with cationic species was first observed in the case of guanidium cations that can donate protons for hydrogen bonding leading to the formation of self-assembled “soft” or “flexible” materials. In the case of such soft frameworks based on the guanidium disulfonate system, each sulfonate function possesses three oxygen atoms and six lone pairs that can form six charge-assisted and directional hydrogen bonds with six protons of the flat guanidium cation [5–7]. The relatively weak coordination ability of organosulfonates functions to transition-metal centers makes difficult the displacement of

ligands such as water and facilitates such hydrogen bonding interactions between the guanidinium cations and later on cationic metal complexes [8–10]. In contrast with other anionic functionalities such as organic phosphonates and/or carboxylates that can replace weak ligands, the sulfonates tend to hydrogen-bond to the available proton-donating ligands instead. Several layered frameworks have been described with cobalt-based complexes and various disulfonate anions [11–14].

Nanostructured silica films hosting metal-based transition complexes are interesting for applications in catalysis, for the preparation of optoelectronic devices, or for optical and electrochemical applications [15–18]. As recently demonstrated, the versatility of the combination of the electrochemically assisted self-assembly (EASA) route to mesoporous silica films [19–21] and click chemistry applied to silica materials [22,23] can be exploited to accommodate polypyridyl metal-based transition metal complexes (e.g.  $[\text{Fe}(\text{tpy})_2]^{2+}$  [24] and  $[\text{Fe}(\text{bpy})_3]^{2+}$  [25]) in such nanostructured materials. In both cases, the immobilization required several steps: (i) generation of azide-functionalized vertically oriented silica films by EASA using tetraethoxysilane (TEOS) and 3-azidopropyltriethoxysilane (AzPTES) as silane precursors; (ii) grafting of the polypyridyl ligands by click coupling with a specifically prepared ethynyl polypyridyl derivative; (iii) coordination of  $\text{Fe}^{2+}$  ions to the polypyridyl-functionalized silica films by dipping the films in an aqueous solution containing  $\text{FeSO}_4 \cdot \text{H}_2\text{O}$ ; (iv) the coordination sphere of the iron (II) was completed by dipping the films in a solution containing bipyridine or terpyridine ligands in acetonitrile to form the final transition-metal coordination complexes [24,25].

The aim of the present work is to propose an alternative to the above time-consuming covalent approach for the immobilization of transition-metal coordination complexes in vertically oriented silica films, based on the use of sulfonate-functionalized silica films as weak coordinating membranes allowing the immobilization of  $\text{Fe}^{2+}$  centers in a first step. Two distinct hypotheses should be considered to explain the immobilization mechanism of  $\text{Fe}^{2+}$  centers in the first stage of the modification process: (i) the organosulfonate moieties could act as a second coordination sphere interacting via the formation of hydrogen bonds with the aquo ligands of the  $[\text{Fe}(\text{H}_2\text{O})_6]^{2+}$  complex; (ii) direct weak coordination of the organosulfonate functions to the  $\text{Fe}^{2+}$  centers to form the  $[\text{Fe}(\text{SO}_3\text{-R})_2(\text{H}_2\text{O})_4]^{2+}$  moieties. In both cases, such interactions are obviously weaker than a covalent bond but are strong enough to avoid the spontaneous leakage of the coordination complexes immobilized in the first step of the functionalization process. Then, we demonstrate the ability of organosulfonate to act as a weak coordinating ligand to bind iron (II) cations that can subsequently react with bipyridine ligands to form and immobilize polypyridine complexes in situ in such nanoporous matrices. We finally explore the optical and electrochemical properties of the synthesized  $[\text{Fe}(\text{bpy})_3]^{2+}\text{SO}_3^-@ \text{SiO}_2$  films. This work opens the door to the application of such a modification strategy for the immobilization of other species that cannot be easily introduced into the silica matrix by the covalent route.

## 2. Results and Discussion

### 2.1. Generation of Mesoporous Films and Monitoring of the Successive Functionalization Steps

The internal surface of the oriented nanochannels of the mesoporous silica films is negatively charged (due to the presence of silanolate groups at pH higher than the isoelectric point of silica, i.e., 2) [21,26,27]. Therefore, it could in principle be exploited for binding positively charged complexes as  $[\text{Fe}(\text{bpy})_3]^{2+}$  via favorable electrostatic interactions. This could be an alternative strategy to the covalent immobilization of transition metal-based cationic complexes in mesoporous silica films that we used previously for confining  $[\text{Fe}(\text{bpy})_3]^{2+}$  and  $[\text{Fe}(\text{terpy})_2]^{2+}$  in similar mesoporous silica films. However, all attempts to implement this electrostatic immobilization approach to non-functionalized vertically aligned mesoporous silica films prepared by EASA have been unsuccessful in spite of mesopore size (i.e., 2 nm in diameter) larger than the probe size (i.e., 0.8 nm for  $[\text{Fe}(\text{bpy})_3]^{2+}$ ). Cyclic voltammetry experiments (which are commonly used to point out accumulation effects in such films [28]) have not shown any evidence of the presence of those electroactive

species accumulated in the nanoporous matrices (see Figure S1) suggesting that their effective immobilization would require significantly stronger interactions than the “simple” electrostatic ones with the negatively charged silanolate groups.

Based on these observations, a weak coordinating group, i.e., propylsulfonate, has been employed to firstly immobilize  $\text{Fe}^{2+}$  ions in the nanopores of the oriented silica thin films. To this aim, the vertically oriented silica thin films containing mercaptopropyl functions (Figure 1A1) have been electrochemically generated on ITO electrodes by adapting the previously reported EASA procedure [20,29], using this time TEOS and MPTMS as silane and organosilane precursors. It has been previously demonstrated that a high level of ordering can be obtained for vertically oriented mercaptopropyl-functionalized films prepared by EASA, with hexagonally packed and oriented mesochannels maintained intact in the nanostructure up to 30% MPTMS in the starting sol [30], which is also the case here (Figure 1A2). Then, these grafted thiol functions have been chemically oxidized by dipping the mercaptopropyl-functionalized films in an acidic solution of hydrogen peroxide (Figure 1B). This medium is indeed known to enable the effective oxidation of thiol groups into sulfonate moieties, even in a confined environment as that of silica mesochannels, as confirmed by Raman spectroscopy and XPS [31–33]. The sulfonate functionalized films were subsequently dipped in a solution containing 10 mM  $\text{FeSO}_4 \cdot 7\text{H}_2\text{O}$ , a medium where all the iron (II) sulfate species dissolved in water to form the corresponding aquo complex,  $[\text{Fe}(\text{H}_2\text{O})_6]^{2+}$  (with octahedral molecular geometry), likely to interact with sulfonate moieties (Figure 1C1). Cyclic voltammetry and XPS analysis were employed to prove the presence of iron (II) inside the mesoporous channels. The electrochemical response obtained is shown in Figure 1C2 exhibiting oxidation and reduction peaks around 0.5 V vs. Ag/AgCl assigned to the  $[\text{Fe}(\text{H}_2\text{O})_6]^{2+/3+}$  redox system in the silica matrix (XPS analysis will be discussed hereafter). The last step of the functionalization process consisted of the displacement of the aquo ligands by bipyridine molecules completing the coordination sphere of the transition metal (this was achieved by dipping the modified silica film in a 30 mM solution of bipyridine ligands in acetonitrile) to form  $[\text{Fe}(\text{bpy})_3]^{2+}$  interacting with sulfonate moieties (Figure 1D1). Figure 1D2 shows the oxidation/reduction signals characteristic of the resulting  $[\text{Fe}(\text{bpy})_3]^{2+}\text{SO}_3^- @\text{SiO}_2$ , appearing at more positive potentials due to the change of coordination sphere of the iron center, in good agreement with the electrochemical behavior previously described for  $[\text{Fe}(\text{bpy})_3]^{2+}$  covalently attached to the silica walls [25].

XPS analysis of the functionalized mesoporous silica films was performed in order to follow the successive functionalization steps and quantify the film composition at each of these (see Figure S2). As an example, the XPS survey spectrum obtained for a 20/80 mercaptopropyl-functionalized silica film is given in supporting information. It shows the C1s (285 eV), O1s (532 eV), S2s (230 eV), S2p (162 eV) and Si2p (100 eV) characteristic peaks (Figure S2d). The S2s and S2p core level spectrum can be used to monitor the chemical oxidation of the mercaptopropyl functions inside the nanopores. Figure 2 shows the evolution of the S2p core level spectrum before (Figure 2A) and after 10 and 30 min of chemical oxidation using hydrogen peroxide (Figure 2B,C, respectively). In Figure 2A, the S2p core level spectrum shows an asymmetric peak at  $161.6 \pm 0.2$  eV assigned to the thiol groups [30]. The presence of such not very well-resolved doublet is attributed to the low sulfur content in the sample [34]. As is expected, the amount of reduced sulfur (thiol, -SH) decreases progressively during chemical oxidation with hydrogen peroxide, and a new S2p peak appears centered at 167 eV attributed to the oxidized form of sulfur into sulfonate,  $\text{SO}_3^-$ . After 10 min of chemical oxidation, about 50% of the initial thiol functions are transformed into sulfonate (Figure 2B) whereas after 30 min the oxidation is quantitative, and all the sulfur is in the form of sulfonate (Figure 2C).

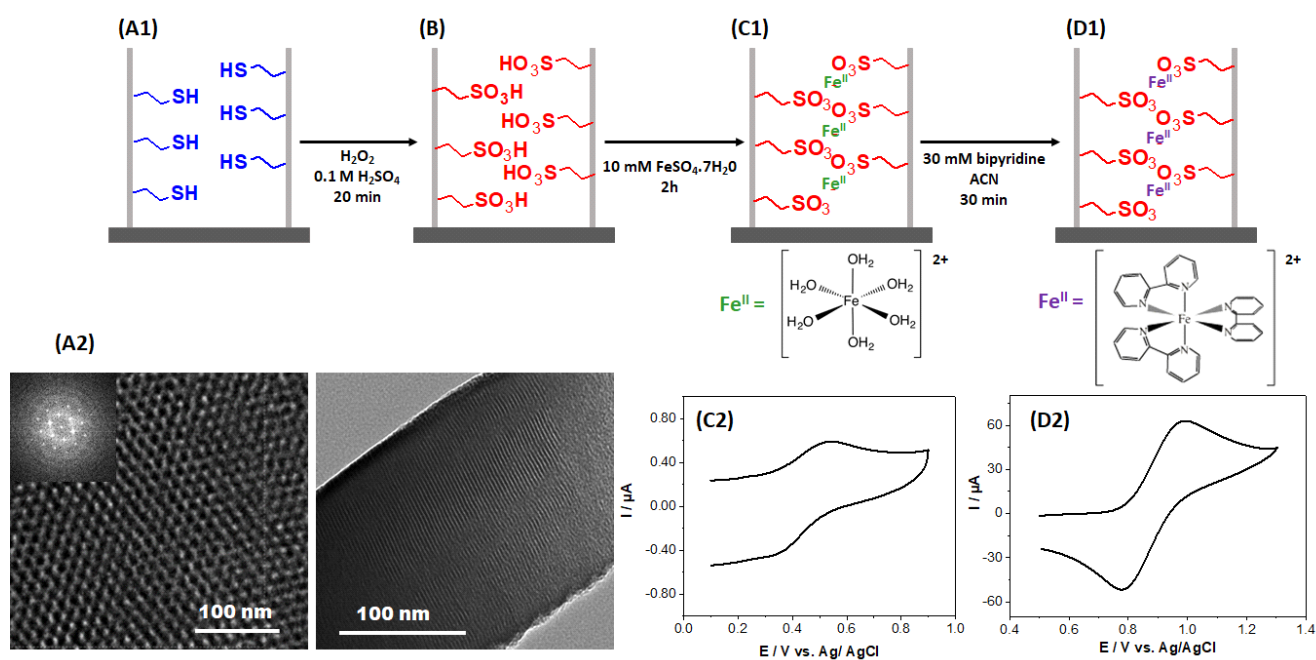


**Figure 1.** (A) Mercaptopropyl-functionalized silica thin films electrochemically obtained by EASA from TEOS and MPTMS as silane precursors ((A1): schematic illustration of one mesopore channel; (A2): TEM top and cross-section views). (B) Chemical oxidation of the mercaptopropyl functions into propylsulfonate using a solution of hydrogen peroxide in 0.1 M  $\text{H}_2\text{SO}_4$ . (C1) Immobilization of  $[\text{Fe}(\text{H}_2\text{O})_6]^{2+}$  in sulfonated-functionalized silica films by immersion in an aqueous solution containing 10 mM  $\text{FeSO}_4 \cdot 7\text{H}_2\text{O}$  for 2 h in an inert atmosphere ((C1): illustrative scheme; (C2): cyclic voltammogram recorded at a scan rate of  $50 \text{ mV s}^{-1}$  in 0.1 M  $\text{NaNO}_3$  aqueous solution). (D) Replacement of the aquo ligands by immersion in an acetonitrile solution containing 30 mM bipyridine ((D1): illustrative scheme; (D2): cyclic voltammogram recorded at a scan rate of  $50 \text{ mV s}^{-1}$  in 0.1 M  $\text{NaNO}_3$  aqueous solution).

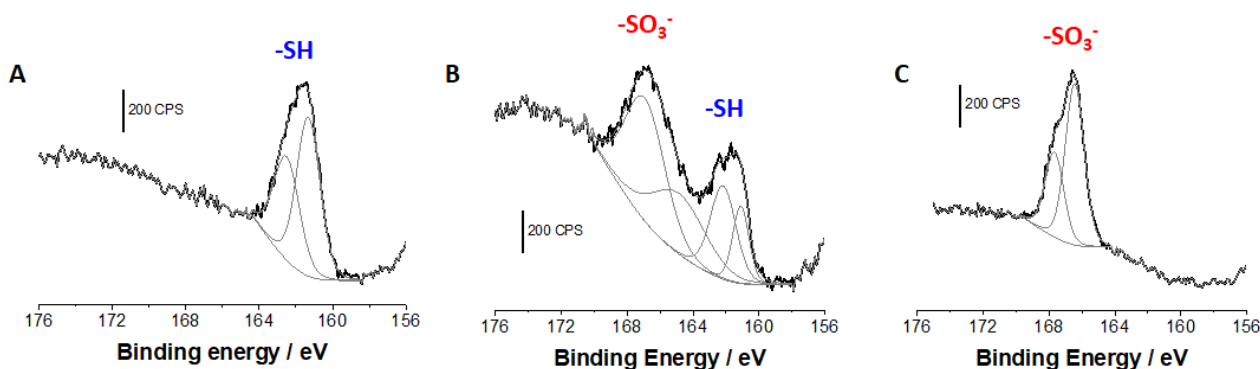


**Figure 2.** S2p core level spectra of a mercaptopropyl-functionalized mesoporous silica film (obtained by EASA from a sol prepared from 20/80 MPTMS:TEOS), respectively, recorded before (A), after 10 min (B), and after 30 min (C) of chemical oxidation with hydrogen peroxide (30%) in 0.1 M  $\text{H}_2\text{SO}_4$ .

The next step of the functionalization process consisted in the coordination of  $\text{Fe}^{2+}$  in the sulfonate-functionalized silica films ( $\text{Fe}^{2+}\text{SO}_3^-@ \text{SiO}_2$ ). This was also characterized by XPS to determine the iron loadings as a function of the composition of the films. The survey spectra were recorded on different spots for each modified film and the average values of atomic composition and binding energy are gathered in Table 1. For  $\text{Fe}^{2+}\text{SO}_3^-@ \text{SiO}_2$  films, Fe2p peaks appeared in addition to C1s (285 eV), O1s (532 eV), S2p (167 eV), and Si2p (100 eV) (Figure S2b), and they grew evidently with the sulfonate content in the material (Table 1). Figure 3 displays the narrow S2p (left), Fe2p (center), and N1s (right) core level

spectra obtained with 20/80 films, respectively, for  $\text{SO}_3^-@SiO_2$  (top),  $\text{Fe}^{2+}\text{SO}_3^-@SiO_2$  (middle), and  $[\text{Fe}(\text{bpy})_3]^{2+}\text{SO}_3^-@SiO_2$  (bottom). For  $\text{Fe}^{2+}\text{SO}_3^-@SiO_2$ , the main envelope of the Fe2p curve fitted with Fe2p3/2 and Fe2p1/2 peaks centered at 710.7 and 723.5 eV, respectively, corresponding well to the presence of  $\text{Fe}^{2+}$ . On the other hand, the interaction of the iron with the sulfonate moieties leads to a shift of 0.5 eV of the binding energy values corresponding to the peaks observed in the S2p core level spectrum due to a change in the sulfonate environment. The resulting S/Fe atomic ratios were close to 2 (Table 1), suggesting the binding of one  $\text{Fe}^{2+}$  to two  $\text{SO}_3^-$ , consistent with the charge balance. The last step of the modification process involved the displacement of aqueous ligands by bipyridine resulting in a change in the coordination sphere of the metal center with the in situ formation of the  $[\text{Fe}(\text{bpy})_3]^{2+}$ . In this last step, the sulfonate stops acting as a weak ligand in the second coordination sphere of the iron and behaves as a counter ion in the  $[\text{Fe}(\text{bpy})_3]^{2+}\text{SO}_3^-@SiO_2$  material. Furthermore, the presence of bipyridine ligands and the in situ formation of the  $\text{Fe}(\text{bpy})_3^{2+}$  is demonstrated by the emerging N1s component at 399.5 eV attributed to the bipyridine ligands, with N/Fe atomic ratios close to 6 (Table 1) in agreement with the stoichiometry of the  $[\text{Fe}(\text{bpy})_3]^{2+}$  complex, confirming the success of its formation in the  $[\text{Fe}(\text{bpy})_3]^{2+}\text{SO}_3^-@SiO_2$  films prepared with concentrations of silica precursors up to 20/80 MPTMS/TEOS. Increasing further the amount of organic groups in the mesopore channels results in a higher degree of occupation of the space available inside the matrix making difficult the replacement of aquo ligands by the bulky bipyridine moieties in the last step of the modification process which is evidenced by the significant decrease in the N/Fe ratio for the 30/70 MCTMS/TEOS films.

**Table 1.** Atomic composition (% At.) and binding energies (BE) for the functionalized mesoporous silica films at each step of the modification process (data obtained from the XPS measurements).

Films Composition	Si2p Signal		S2p Signal		Fe2p Signal		N1s Signal		Atomic Ratios		
	%At	BE/Ev	%At	BE/Ev	%At	BE/Ev	%At	BE/Ev	S/Si	S/Fe	N/Fe
MCTMS/TEOS											
5/95	95.8	102.0	4.2	161.7	----	----	----	----	0.04	----	----
10/90	90.5	102.0	9.5	161.7	----	----	----	----	0.11	----	----
20/80	81.2	102.0	18.8	161.8	----	----	----	----	0.23	----	----
30/70	72.3	102.0	27.7	161.7	----	----	----	----	0.38	----	----
$\text{SO}_3^-/\text{TEOS}$											
5/95	96.0	102.0	4.0	167.1	----	----	----	----	0.04	----	----
10/90	96.7	102.0	9.3	167.2	----	----	----	----	0.10	----	----
20/80	81.6	102.0	18.4	167.2	----	----	----	----	0.23	----	----
30/70	71.5	102.0	28.5	167.2	----	----	----	----	0.40	----	----
$\text{Fe}^{2+}\text{SO}_3^-/\text{TEOS}$											
5/95	94.3	102.0	3.8	167.7	1.9	710.7/723.4	---	----	0.04	2.00	----
10/90	88.1	102.0	8.5	167.7	3.7	710.8/723.5	---	----	0.10	2.30	----
20/80	79.9	102.0	14.2	167.8	5.9	710.7/723.4	---	----	0.18	2.41	----
30/70	69.9	102.0	23.1	167.8	7.0	710.7/723.4	---	----	0.33	3.30	----
$[\text{Fe}(\text{bpy})_3]^{2+}\text{SO}_3^-/\text{TEOS}$											
5/95	87.5	102.0	2.9	167.5	1.4	710.7/723.4	8.2	399.9	0.03	2.10	5.86
10/90	74.7	102.0	5.9	167.4	2.9	710.8/723.4	16.5	399.8	0.08	2.03	5.69
20/80	48.5	102.0	11.1	167.4	5.5	710.9/723.3	31.9	399.7	0.23	2.02	5.80
30/70	65.3	102.0	22.5	167.4	6.1	710.9/723.4	6.1	399.8	0.34	3.69	1.00

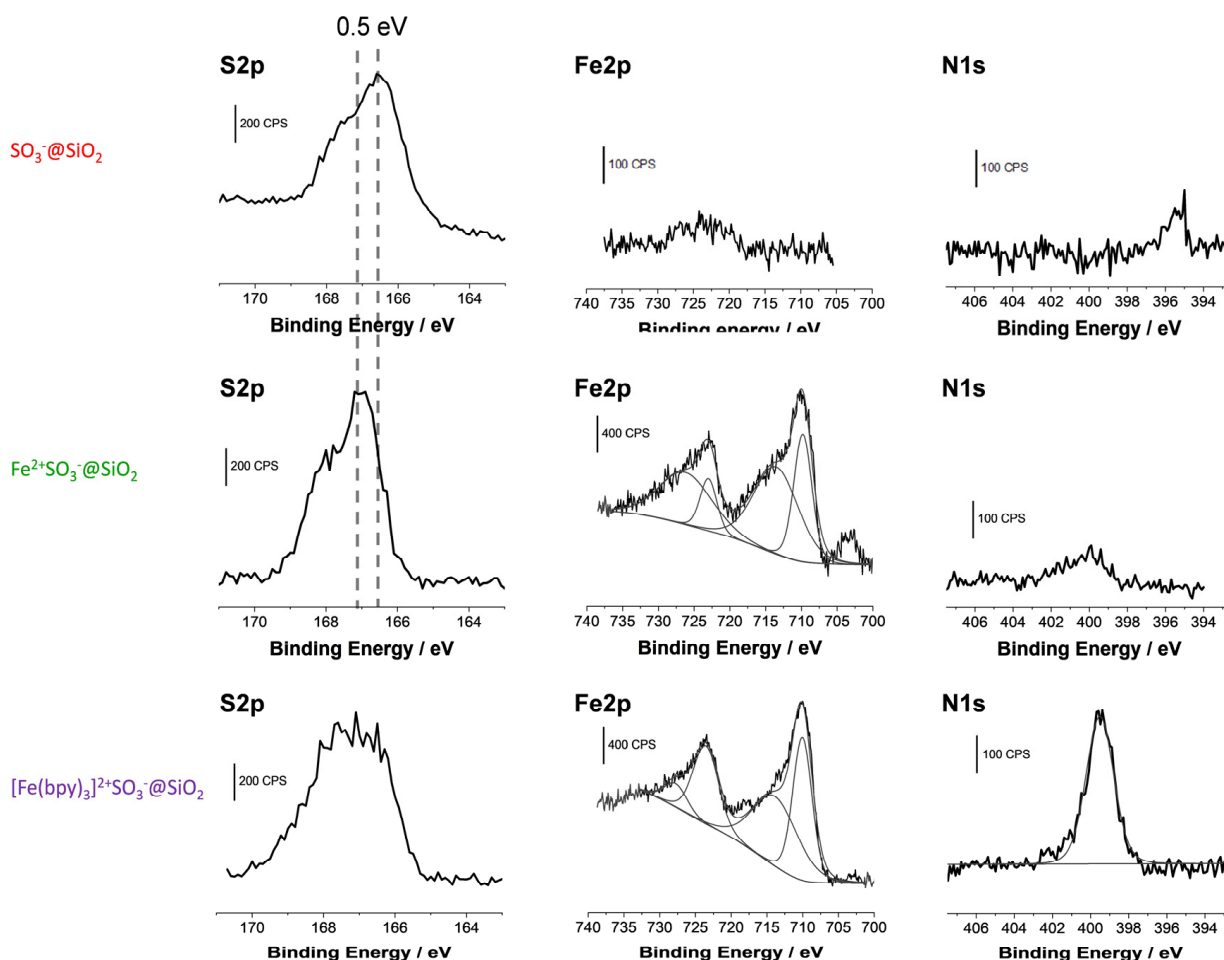


**Figure 3.** S2p (left), Fe2p (center) and N1s (right) core level spectra recorded for 20/80 films, respectively, functionalized with sulfonate groups ( $\text{SO}_3^-@SiO_2$ , top), after complexation with iron (II) ( $\text{Fe}^{2+}\text{SO}_3^-@SiO_2$ , middle) and after  $\text{Fe}^{2+}$  complexation and bipyridine displacement of aquo ligands ( $[\text{Fe}(\text{bpy})_3]^{2+}\text{SO}_3^-@SiO_2$ , bottom).

## 2.2. Structural Characterization of $[\text{Fe}(\text{bpy})_3]^{2+}$ Complexes Formed in the Films

Structural characterization of the  $[\text{Fe}(\text{bpy})_3]^{2+}$  complex confined in silica films was performed by resonance Raman spectroscopy, measured in the  $[100\text{--}1800] \text{ cm}^{-1}$  range as depicted in Figure 4. The spectra have been obtained under resonance conditions with the metal(d)  $\rightarrow$  bpy(\*) metal-to-ligand charge transfer (MLCT) absorption band using 532 nm excitation, therefore enhancing vibrational modes which are vibronically active in the corresponding electronic transition. For comparison purposes, and for identification of the exact complexes that were formed in situ in the silica films, we can use the Raman spectrum obtained previously on covalently attached  $[\text{Fe}(\text{bpy})_3]^{2+}$  complexes in ordered silica thin films [25] as a benchmark.

The Raman spectrum of  $[\text{Fe}(\text{bpy})_3]^{2+}$  and corresponding vibration modes can be separated into three categories: ring modes, inter-ring vibrations (within a bipyridine ligand), and metal–ligand modes. In the  $1100\text{--}1610 \text{ cm}^{-1}$  wavenumber range, the Raman spectrum is strongly dominated by bands arising from the skeletal stretching vibrations of the bpy ligands. This indicates that the electron transfer is extensively delocalized over the aromatic ring system [35]. In particular, the mode at  $1489 \text{ cm}^{-1}$  is attributed to the C=C stretching mode, the bands at  $1275$ ,  $1322$ , and  $1562 \text{ cm}^{-1}$  correspond to the C-H bending mode [36], while the C=N stretching mode is located at  $1605 \text{ cm}^{-1}$ . This is consistent with the assignment of vibrational bands for  $[\text{Fe}(\text{bpy})_3]^{2+}$  and  $[\text{Ru}(\text{bpy})_3]^{2+}$  proposed in the literature from resonant Raman, infrared, and DFT calculations [36–40]. The bands observed

at 662, 766, and 1022  $\text{cm}^{-1}$  are characteristic of ring deformation. The 155  $\text{cm}^{-1}$  frequency has been attributed to a combination of chelate-ring modes, benzene cycle bending modes, and N-Fe-N bending modes. The observed band at 369  $\text{cm}^{-1}$  corresponds to the Fe-N stretching mode [41]. The complete corresponding band wavenumbers and proposed assignments are summarized in Table 2. Otherwise, the resonance Raman spectra of  $[\text{Fe}(\text{bpy})_3]\text{SO}_4 \cdot 7.5\text{H}_2\text{O}$  microcrystalline powder and  $[\text{Fe}(\text{bpy})_3]^{2+}/\text{SO}_3^-@/\text{SiO}_2$  are perfectly overlapped, thus indicating that the structure of the  $[\text{Fe}(\text{bpy})_3]^{2+}$  complex is maintained within the silica. Additionally, the complete Raman spectrum of  $[\text{Fe}(\text{bpy})_3]^{2+}$ , whether it is immobilized in the mesoporous silica thin film through covalent interactions (our previous work [25]) or through hydrogen bonds (the present work), is almost identical with marginal band shift (at maximum 2–3  $\text{cm}^{-1}$ ). This allows to confirm that in both cases, as deeply discussed in [25], the confined complex  $[\text{Fe}(\text{bpy})_3]$  is in the formal 2+ oxidation state, and LS electronic state. This is proved by the frequency of the Fe-N stretching mode, observed at 369  $\text{cm}^{-1}$ . This band would shift to nearly 200–250  $\text{cm}^{-1}$  for the Fe(II) in the HS state [41–45].

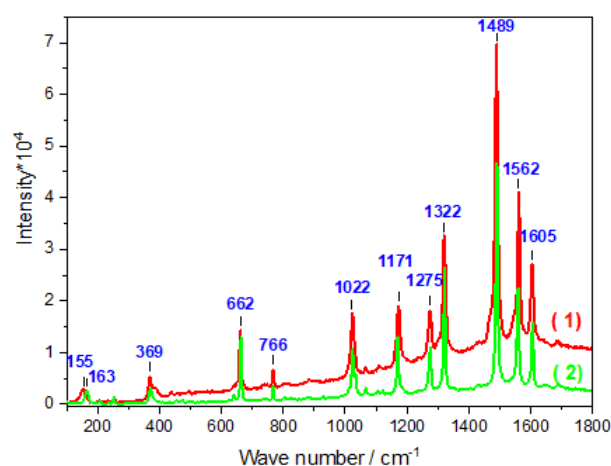


**Figure 4.** Comparison of the Raman spectra of  $[\text{Fe}(\text{bpy})_3]^{2+}\text{SO}_3^-@/\text{SiO}_2$  film (red, 1) and the Raman spectra of  $[\text{Fe}(\text{bpy})_3]\text{SO}_4 \cdot 7.5\text{H}_2\text{O}$  microcrystalline powder (green, 2).

**Table 2.** Identified Raman vibration modes and assignment for  $[\text{Fe}(\text{bpy})_3]^{2+}\text{SO}_3^-@/\text{SiO}_2$ .

Peak Position ( $\text{cm}^{-1}$ )	Assignment
155	$\delta$ (N-Fe-N); benzene cycle bending modes
369	$\nu$ (Fe-N)
662	Ring deformation
766	Ring deformation
1022	Ring deformation
1275	$\delta$ (C-H)
1322	$\delta$ (C-H)
1489	$\nu$ (C=C)
1562	$\delta$ (C-H)
1605	$\nu$ (C=N)

### 2.3. Electrochemical Response of the $[\text{Fe}(\text{bpy})_3]^{2+}\text{SO}_3^-@/\text{SiO}_2$ Films

Figure 5 shows the evolution of the electrochemical response obtained by cyclic voltammetry (CV) for four mesoporous silica films bearing  $[\text{Fe}(\text{bpy})_3]^{2+}$  at various functionalization degrees (5, 10, 20, and 30% organosilane) recorded in an aqueous 0.1 M  $\text{NaNO}_3$  solution at scan rates varying from 10 to 70  $\text{mV s}^{-1}$ . The cyclic voltammograms are related to the  $[\text{Fe}(\text{bpy})_3]^{2+/3+}$  redox couple centered at 0.87 V vs. Ag/AgCl. CV curves clearly exhibit an evolution related to the functionalization degree. An increase in the anodic and cathodic peak current values is observed with increasing the level of functionalization

from 5% up to 20% of sulfonate groups (see left of Figure 5, from D to B), as a result of increasing amounts of  $[\text{Fe}(\text{bpy})_3]^{2+}$  in the film. As a matter of fact, a higher concentration of sulfonate groups results in a higher amount of immobilized  $[\text{Fe}(\text{bpy})_3]^{2+}$  species, and therefore a more intense electrochemical response. Above this 20% value (i.e., highlighted for 30% of sulfonate groups in the film), the peak currents dropped significantly (Figure 5A). One plausible explanation for this observation is the lack of free space for  $[\text{Fe}(\text{bpy})_3]^{2+}$  to form in the mesoporous channels due to steric hindrances when larger amounts of organosulfonate groups are initially present in the starting film, leading to the formation of a lower amount of  $[\text{Fe}(\text{bpy})_3]^{2+}$  units under these conditions. The optimal situation corresponding to the largest currents is thus that corresponding to the film prepared using a 20/80 MPTMS/TEOS ratio. For this film, a charge of 236  $\mu\text{C}$  can be extracted from the integration of the anodic signal, corresponding to  $18.6 \times 10^{-10}$  mol  $[\text{Fe}(\text{bpy})_3]^{2+}$ . It is noteworthy that CVs were stable upon multiple successive potential scans (yet with a small intensity decrease in the first 10–15 cycles, which might be due to some loss of loosely bonded  $[\text{Fe}(\text{bpy})_3]^{2+}$  species, but after that the CV curves remained identical for at least 50 cycles). All curves displayed in Figure 5 have been obtained in conditions of steady-state response. In all cases, peak currents were directly proportional to the square root of the potential scan rate, indicating that the overall charge transfer processes are diffusion controlled. Indeed, for redox probes immobilized in such insulating mesoporous silica films, their overall electrochemical response is diffusion-controlled, either limited by the pseudo-diffusion of electrons hopping from one redox site to another, or by the diffusion of charge-compensating counter-ions, or a mixture of both processes [46]. No significant difference in the variations of peak potentials with the potential scan rate was observed from one film to another one, suggesting that charge transfer kinetics are not really affected by the amount of  $[\text{Fe}(\text{bpy})_3]^{2+}$  species in the films. This appears as an advantage compared to covalently bonded redox moieties in mesoporous silica films (e.g., ferrocene functionalized ones) for which significant charge transfer limitations at low loadings have been reported [46].

#### 2.4. Optical Properties of $[\text{Fe}(\text{bpy})_3]^{2+}$ Modified Sulfonated Silica Films

Further evidence of the in situ formation of the  $[\text{Fe}(\text{bpy})_3]^{2+}$  complex is the coloration change of the  $\text{Fe}^{2+}\text{SO}_3^-@ \text{SiO}_2$  film when immersed in a 10 mM bipyridine solution in acetonitrile. The optical spectra of  $[\text{Fe}(\text{bpy})_3]^{2+}$  complexes confined in silica films (i.e., the  $[\text{Fe}(\text{bpy})_3]^{2+}\text{SO}_3^-@ \text{SiO}_2$  material) were recorded from 300 to 800 nm (Figure 6), absorption measurement below 300 nm is hindered since transmittance of ITO drops sharply in the ultraviolet region due to its narrow optical band gap [47]. The absorption spectrum exhibits a broad band centered at 527 nm with a shoulder on the high energy side, and a second absorption band centered at 355 nm. They can be assigned to metal-to-ligand charge transfer (MLCT) transitions ( $d(\pi) \rightarrow \pi^*$ ) [48,49]. These MLCT bands depend on the LUMO energy of polypyridyl ligands. They are very similar to the broad bands centered at 350 and 520 nm, characteristic of  $[\text{Fe}(\text{bpy})_3]^{2+}$  in aqueous solution, and located at absorption wavelength values consistent with those of the literature [50]. The slight shift observed for  $[\text{Fe}(\text{bpy})_3]^{2+}\text{SO}_3^-@ \text{SiO}_2$  compared to the bands of solution-phase  $[\text{Fe}(\text{bpy})_3]^{2+}$  complexes is attributed to confinement effects in the silica matrix [51,52]. An additional sharp absorption increase at lower wavelengths is also noticeable and it can be related to the intense absorption band around 300 nm observed for  $[\text{Fe}(\text{bpy})_3]^{2+}$  in solution corresponding to ligand-centered transitions ( $\pi \rightarrow \pi^*$ ) of the coordinated bpy ligands [53]. As a control experiment, recording the absorption spectrum for the  $\text{SO}_3^-@ \text{SiO}_2$  films did not show any bands in the visible region, confirming that the bands observed for  $[\text{Fe}(\text{bpy})_3]^{2+}\text{SO}_3^-@ \text{SiO}_2$  (Figure 6) are intrinsic to  $[\text{Fe}(\text{bpy})_3]^{2+}$  species confined in the film, and not to the sulfonate functionalized silica film itself. Additionally, the present absorption spectrum for  $[\text{Fe}(\text{bpy})_3]^{2+}\text{SO}_3^-@ \text{SiO}_2$  is very similar to the corresponding spectrum previously measured for  $[\text{Fe}(\text{bpy})_3]^{2+}$  complexes covalently attached to mesoporous silica

thin film [25], suggesting that the way of immobilization does not significantly affect the properties of metal complexes in the confined environment of mesopore channels.

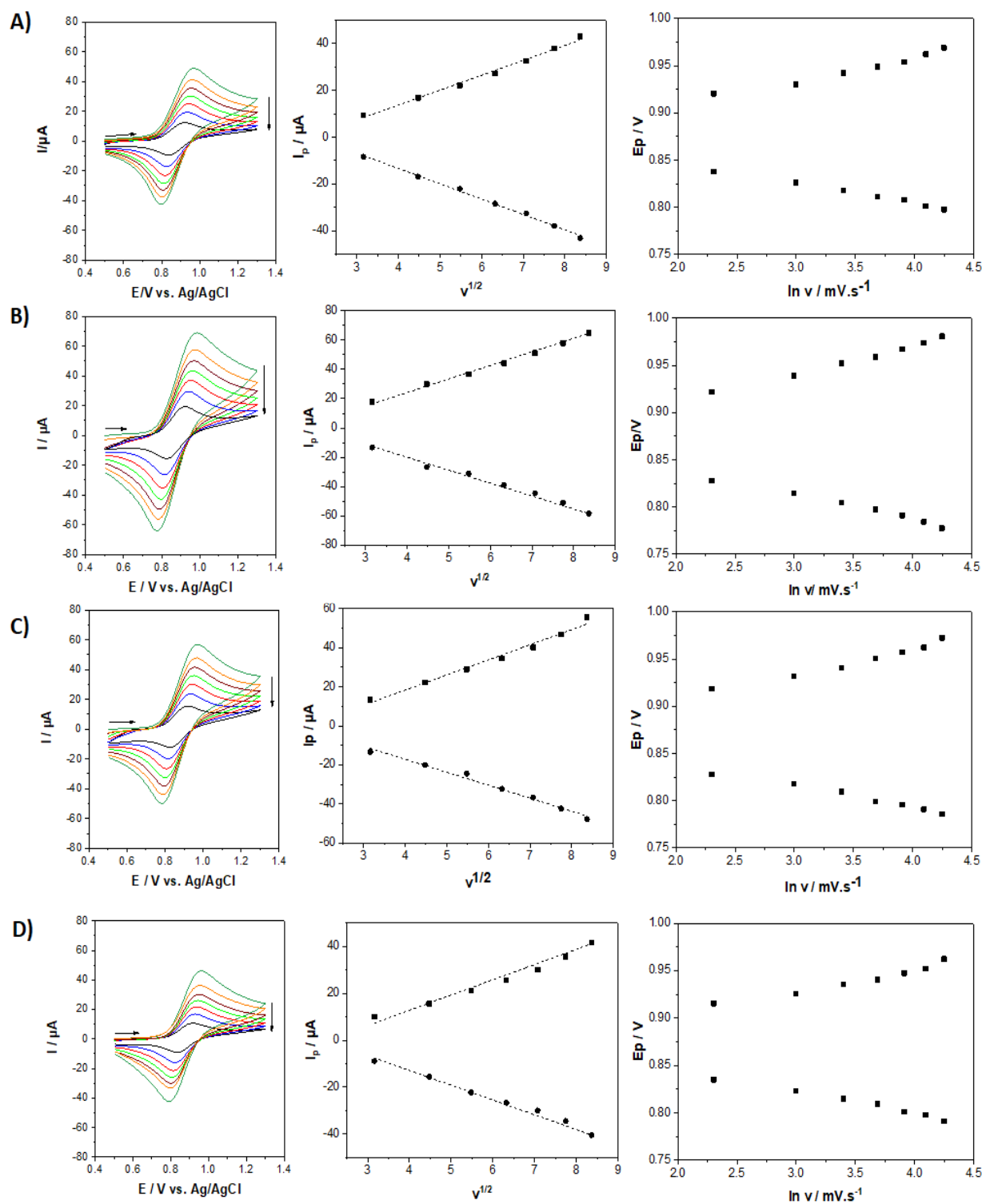


**Figure 5.** Cyclic voltammograms of  $[\text{Fe}(\text{bpy})_3]^{2+}\text{SO}_3^-@ \text{SiO}_2$  functionalized films recorded at potential scan rates of 10, 20, 30, 40, 50, 60, and 70  $\text{mV}\cdot\text{s}^{-1}$  in an aqueous electrolyte solution containing 0.1 M  $\text{NaNO}_3$ . Left: CVs of the films prepared from various MPTMS/TEOS ratios (total concentration of silane precursors: 200 mM): 30/70 (A); 20/80 (B); 10/90 (C); 5/95 (D). Middle: Dependence of the peak current with the square root of the potential scan rate. Right: Evolution of peak potentials as a function of the logarithm of potential scan rate.

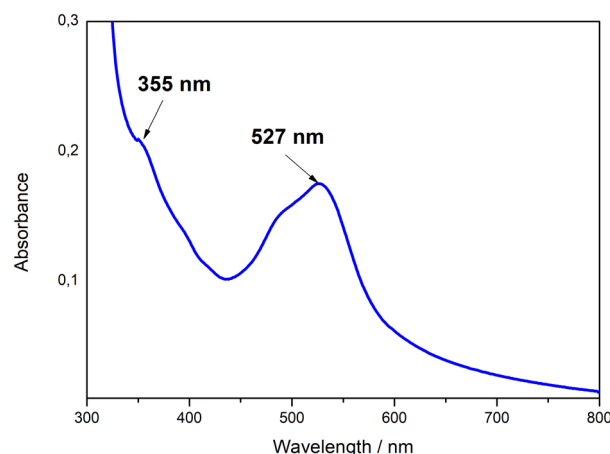


**Figure 6.** UV-Vis absorption spectrum of a 20/80 MPTMS/TEOS films after immobilizing  $[\text{Fe}(\text{bpy})_3]^{2+}$ .

### 3. Materials and Methods

#### 3.1. Apparatus

All the electrochemical experiments were performed using a  $\mu\text{AutoLab III}$  potentiostat (Eco Chemie) monitored by the GPES software. A three-electrode configuration was employed for all the electrochemical measurements in a one-compartment cell. The voltammetric curves were recorded using a platinum rod as a counter electrode, Ag/AgCl as a reference electrode (Metrohm), and ITO plates (from Delta Technologies; surface resistivity: 8–12  $\Omega$ ) as working electrodes where the hybrid films were previously deposited. The electrochemically assisted deposition was carried out using a homemade electrochemical cell with a configuration allowing placing the working electrode at the bottom [54]. A stainless-steel counter electrode and a silver wire as a pseudo-reference electrode completed the electrochemical setup.

Several physico-chemical techniques were used to characterize the materials. The mesostructure, morphology, and thickness of the films have been analyzed by transmission electron microscopy (TEM) using an ACCEL ARM 200F microscope at an acceleration voltage of 200 kV. X-ray photoelectron spectroscopy (XPS) characterizations were performed using a KRATOS Axis Ultra X-ray photoelectron spectrometer (Kratos Analytical, Manchester, UK) equipped with a monochromated  $\text{AlK}\alpha$  X-ray source ( $h\nu = 1486.6$  eV) operated at 150 W. Raman spectra were recorded using a confocal Raman microscope (inVia<sup>®</sup> Qontor with a Peltier-cooled CCD camera, Renishaw, Wotton-under-Edge, UK) equipped with a 532 nm laser (irradiance  $< 5$   $\text{kW cm}^{-2}$ ), a 50 $\times$  objective with a numerical aperture of 0.55, and a 1200 lines. $\text{mm}^{-1}$  grating. The spectral resolution was about 3  $\text{cm}^{-1}$  (10 acquisitions of 4 s). Each sample was analyzed at different points to verify the homogeneity of the studied functionalized silica films. The laser power was optimized to 0.5 mW and the spectrum was recorded in the 50 to 4000  $\text{cm}^{-1}$  wavenumber range. The optical absorption spectra were obtained using a Carry 60 UV-Vis spectrophotometer.

#### 3.2. Chemicals and Reagents

Tetraethoxysilane (TEOS, 98%, Alfa Aesar), 3-mercaptopropyltrimethoxysilane (MPTMS, 95%, Alfa Aesar), cetyltrimethylammonium bromide (CTAB, 99%, Acros), sodium nitrate ( $\text{NaNO}_3$ , 99.5%, Prolabo), iron (II) sulfate heptahydrate ( $\text{FeSO}_4 \cdot 7\text{H}_2\text{O}$ , 99%, Aldrich), 2,2'-Bipyridyl (Bpy, 99%, Aldrich), ethanol (95–96%, Merck), hydrochloric acid (37%, Riedel de Haen), and anhydrous acetonitrile (ACN, 99.8%, Aldrich) were used as received without further purification.

#### 3.3. Preparation of Thiol and Sulfonate Functionalized Silica Films

Sulfonate-modified silica thin films have been synthesized in two steps involving firstly the synthesis of thiol-modified silica films ( $\text{MPTMS}@SiO_2$ ) followed by their oxidation

using hydrogen peroxide as a chemical oxidizing agent to give the corresponding sulfonate-modified films ( $\text{SO}_3^-@SiO_2$ ).

The synthesis of  $\text{MPTMS}@SiO_2$  has been achieved by slightly modifying the method reported for non-functionalized films (200 mM TEOS in starting sol) using the EASA method and ITO electrode [20]. The starting sol was constituted in this case of a hydroalcoholic solution (water/ethanol (1:1)) containing 160 mM TEOS, 40 mM MPTMS and CTAB as surfactant template (ratio CTAB/TEOS = 0.32) and 0.1 M  $\text{NaNO}_3$  as supporting electrolyte. The pH of the solution was adjusted to 3 using a 0.1 M HCl aqueous solution. The solution was stirred at room temperature for 2.5 h. Then, a cathodic potential (−1.3 V) was applied for 20 s in a three-electrode system using ITO as a working electrode, in order to deposit the thiol-functionalized vertically oriented film. The electrode was thoroughly rinsed with distilled water and deposited in an oven at 130 °C overnight. The synthesis described above refers to an MPTMS/TEOS concentration ratio of 20%. The same methodology has been used to prepare silica films while varying the MPTMS/TEOS concentration ratio in the starting sol (respectively, 5/95, 10/90, 20/80, and 30/70 MPTMS/TEOS molar ratios were used here). The surfactant (CTAB) was extracted from the mesoporous silica films by immersing them in an ethanol solution containing 0.1 M HCl for 20 min. After surfactant removal, the films were rinsed with distilled water. The sulfonate-functionalized films were obtained by chemical oxidation of the thiol moieties, which was achieved by dipping the thiol-functionalized silica films for 30 min in a solution containing  $\text{H}_2\text{O}_2$  (30%) in 0.1 M  $\text{H}_2\text{SO}_4$  (known to promote the oxidation of thiol groups into sulfonate moieties in mesoporous materials [55]).

### 3.4. Preparation of $\text{Fe}(\text{bpy})_3^{2+}\text{SO}_3^-@SiO_2$

The immobilization of  $[\text{Fe}(\text{bpy})_3]^{2+}$  complex in the silica nanochannels was done by successive impregnation of sulfonate functionalized mesoporous silica films, respectively, in an aqueous solution of 10 mM  $\text{FeSO}_4 \cdot 7\text{H}_2\text{O}$  (for 2 h under nitrogen atmosphere in order to avoid the oxidation of the  $\text{Fe}^{2+}$  ions) to form  $\text{Fe}^{2+}\text{SO}_3^-@SiO_2$  and, after rinsing with acetonitrile, by subsequent immersion in a solution containing 30 mM bipyridine in acetonitrile and let reacting for 30 min to generate  $\text{Fe}(\text{bpy})_3^{2+}\text{SO}_3^-@SiO_2$ . A final washing with acetonitrile completed the process.

## 4. Conclusions

In the present work, we have demonstrated that organosulfonate groups grafted to the internal walls of mesoporous silica films can be used as second sphere coordination ligands in the case of first-row transition metal ions that can be used afterwards to form in situ coordination complexes in one step, as demonstrated here for  $\text{Fe}(\text{bpy})_3^{2+}$  species. Their structural, optical, and electrochemical properties are preserved when immobilized in the mesoporous silica matrix. A huge amount of  $\text{Fe}(\text{bpy})_3^{2+}$  species can be confined in the films, up to  $18.6 \times 10^{-10}$  mol for a film prepared from a sol medium with an MPTMS/TEOS ratio of 20/80. The proposed approach could be extended to the confinement of other metal polypyridyl complexes, individually or in a mixture. Such optically and electrochemically active complexes confined in transparent thin films look promising for the development of optical, optoelectronic, or photoswitchable devices.

**Supplementary Materials:** The following supporting information can be downloaded at: <https://www.mdpi.com/article/10.3390/molecules27175444/s1>, Figure S1: Cyclic voltammograms recorded in aqueous 0.1M  $\text{NaNO}_3$  solution after impregnation of a silica film in 10 mM  $\text{FeCl}_3 \cdot 6\text{H}_2\text{O}$  solution for 2 h. The silica film was prepared by EASA method from a solution containing 200 mM of hydrolyzed tetraethoxysilane, 64 mM CTAB and 0.1 M  $\text{NaNO}_3$ .; Figure S2: XPS survey spectra obtained for various functionalized silica films on ITO, respectively, (a)  $[\text{Fe}(\text{bpy})_3]^{2+}\text{SO}_3^-@SiO_2$ , (b)  $\text{Fe}^{2+}\text{SO}_3^-@SiO_2$ , (c)  $\text{SO}_3^-@SiO_2$ , and (d)  $\text{SH}@SiO_2$ .

**Author Contributions:** Methodology, investigation, S.A. and C.R.; resources, C.C.; writing—review and editing, A.W.; conceptualization, writing—review and editing, S.P.; conceptualization, writing—original draft preparation, N.V. All authors have read and agreed to the published version of the manuscript.

**Funding:** This work was mainly funded by the French PIA project “Lorraine Université d’Excellence” (reference ANR-15-IDEX-04-LUE) and the CPER (program SusChemProc). SA acknowledges a PhD fellow from the “Université de Lorraine”.

**Institutional Review Board Statement:** Not applicable.

**Informed Consent Statement:** Not applicable.

**Data Availability Statement:** Not applicable.

**Acknowledgments:** We are grateful to the CNRS, the French PIA project “Lorraine Université d’Excellence” (reference ANR-15-IDEX-04-LUE), and the CPER (program SusChemProc), for financial supports. SA acknowledges a PhD fellow from the “Université de Lorraine”. We are grateful to Dominik Schaniel for fruitful scientific discussions. We also thank Jaafar Ghanbaja for TEM imaging.

**Conflicts of Interest:** The authors declare no conflict of interest.

## References

1. Barton, M.R.; Zhang, Y.; Atwood, J.D. Mono-Sulfonated Derivatives of Triphenylphosphine,  $[\text{NH}_4]\text{TPPMS}$  and  $\text{M}(\text{TPPMS})_2$  ( $\text{TPPMS} = \text{P}(\text{Ph})_2(\text{m-C}_6\text{H}_4\text{SO}_3^-)$ ;  $\text{M} = \text{Mn}^{2+}$ ,  $\text{Fe}^{2+}$ ,  $\text{Co}^{2+}$  and  $\text{Ni}^{2+}$ ). Crystal Structure Determinations for  $[\text{NH}_4][\text{TPPMS}] \cdot \frac{1}{2}\text{H}_2\text{O}$ ,  $[\text{Fe}(\text{H}_2\text{O})_5(\text{TPPMS})]\text{TPPMS}$ ,  $[\text{Co}(\text{H}_2\text{O})_5\text{TPPMS}]\text{TPPMS}$  and  $[\text{Ni}(\text{H}_2\text{O})_6](\text{TPPMS})_4 \cdot \text{H}_2\text{O}$ . *J. Coord. Chem.* **2002**, *55*, 969–983.
2. Li, F.-F.; Ma, J.-F.; Song, S.-Y.; Yang, J.; Liu, Y.-Y.; Su, Z.-M. Influence of Neutral Ligands on the Structures of Silver(I) Sulfonates. *Inorg. Chem.* **2005**, *44*, 9374–9383.
3. Forbes, T.Z.; Sevov, S.C. Metal–Organic Frameworks with Direct Transition Metal–Sulfonate Interactions and Charge-Assisted Hydrogen Bonds. *Inorg. Chem.* **2009**, *48*, 6873–6878. [[CrossRef](#)]
4. Dalrymple, S.A.; Parvez, M.; Shimizu, G.K.H. Supramolecular Encapsulation of Hexaaquo Metal Ions by Second Sphere Coordination. *Chem. Commun.* **2001**, *24*, 2672–2673. [[CrossRef](#)]
5. Holman, K.T.; Pivovar, A.M.; Swift, J.A.; Ward, M.D. Metric Engineering of soft Molecular Host Frameworks. *Acc. Chem. Res.* **2001**, *34*, 107–118. [[CrossRef](#)]
6. Holman, K.T.; Martin, S.M.; Parker, D.P.; Ward, M.D. The Generality of Architectural Isomerism in Designer Inclusion Frameworks. *J. Am. Chem. Soc.* **2001**, *123*, 4421–4431. [[CrossRef](#)]
7. Horner, M.J.; Holman, K.T.; Ward, M.D. Architectural Diversity and elastic Networks in Hydrogen-Bonded Host Frameworks: From Molecular Jaws to Cylinders. *J. Am. Chem. Soc.* **2007**, *129*, 14640–14660. [[CrossRef](#)]
8. Davies, J.A.; Hockensmith, C.A.; Kukushkin, V.Y.; Kukushkin, Y.A. *Synthetic Coordination chemistry: Principles and Practice*; World Scientific: London, UK, 1996.
9. Cote, A.P.; Shimizu, G.H.K. The Supramolecular Chemistry of the Sulfonate Group in Extended Solids. *Coord. Chem. Rev.* **2003**, *245*, 49–64. [[CrossRef](#)]
10. Shimizu, G.H.K.; Vaidhyanathan, R.; Taylor, J.M. Phosphonate and Sulfonate Metal Organic Frameworks. *Chem. Soc. Rev.* **2009**, *38*, 1430–1449. [[CrossRef](#)]
11. Wang, X.Y.; Sevov, S.C. Hydrogen-Bonded Metal-Complex Sulfonate (MCS) Inclusion compounds: Effect of the Guest Molecule on the Host Framework. *Inorg. Chem.* **2007**, *46*, 4626–4631. [[CrossRef](#)]
12. Reddy, S.D.; Duncan, S.; Shimizu, G.K.H. A Family of supramolecular Inclusion solids Based Upon Second-Sphere Interactions. *Angew. Chem. Int. Ed.* **2003**, *115*, 1398–1402. [[CrossRef](#)]
13. Dalrymple, S.A.; Shimizu, G.K.H. An Open Channel Coordination Framework Sustained by Cooperative Primary and Secondary Sphere Interactions. *Chem. Commun.* **2002**, *19*, 2224–2225. [[CrossRef](#)] [[PubMed](#)]
14. Dalrymple, S.A.; Shimizu, G.K.H. Selective Guest Inclusion in a Non-Porous H-Bonded Host. *Chem. Commun.* **2006**, *9*, 956–958. [[CrossRef](#)] [[PubMed](#)]
15. Feinle, A.; Lavoie-Cardinal, F.; Akbarzadeh, J.; Peterlik, H.; Adlung, M.; Wickleder, C.; Huesing, N. Novel Sol–Gel Precursors for Thin Mesoporous  $\text{Eu}^{3+}$ -Doped Silica Coatings as Efficient Luminescent Materials. *Chem. Mater.* **2012**, *24*, 3674. [[CrossRef](#)]
16. Walcarius, A. Mesoporous Materials and Electrochemistry. *Chem. Soc. Rev.* **2013**, *42*, 4098–4140. [[CrossRef](#)]
17. Yamashita, H.; Mori, K.; Kuwahara, Y.; Kamegawa, T.; Wen, M.; Verma, P.; Che, M. Single-Site and Nano-Confined Photocatalysts Designed in Porous Materials for Environmental Uses and Solar Fuels. *Chem. Soc. Rev.* **2018**, *47*, 8072–8096. [[CrossRef](#)]
18. Laskowski, L.; Laskowska, M.; Vilà, N.; Schabikowski, M.; Walcarius, A. Mesoporous Silica-Based Materials for Electronics-Oriented Applications. *Molecules* **2019**, *24*, 2395. [[CrossRef](#)]
19. Walcarius, A.; Sibottier, E.; Etienne, M.; Ghanbaja, J. Electrochemically-Assisted Self-Assembly of Mesoporous Silica Thin films. *Nat. Mater.* **2007**, *6*, 602–608. [[CrossRef](#)]

20. Goux, A.; Etienne, M.; Aubert, E.; Lecomte, C.; Ghanbaja, J.; Walcarius, A. Oriented Mesoporous Silica Films Obtained by Electro-Assisted Self-Assembly. *Chem. Mater.* **2009**, *21*, 731–741. [[CrossRef](#)]
21. Walcarius, A. Electroinduced Surfactant Self-Assembly Driven to Vertical Growth of Oriented Mesoporous Films. *Acc. Chem. Res.* **2021**, *54*, 3563–3575. [[CrossRef](#)]
22. Ziarani, G.M.; Hassanzadeh, Z.; Gholamzadeh, P.; Asadi, S.; Badiei, A. Advances in click chemistry for silica-based material construction. *RSC Adv.* **2016**, *6*, 21979–22006. [[CrossRef](#)]
23. Cattoen, X.; Nouredine, A.; Croissant, J.; Moitra, N.; Burglova, K.; Hodacova, J.; de los Cobos, O.; Lejeune, M.; Rossignol, F.; Toulemon, D.; et al. Click Approaches in Sol-Gel Chemistry. *J. Sol-Gel Sci. Technol.* **2014**, *70*, 245–253. [[CrossRef](#)]
24. Vilà, N.; Walcarius, A. Bis(terpyridine) Iron(II) Functionalized Vertically-Oriented Nanostructured Silica Films: Toward Electrochromic Materials. *Front. Chem.* **2020**, *8*, 830. [[CrossRef](#)]
25. Ahoulou, S.; Vilà, N.; Pillet, S.; Carteret, C.; Schaniel, D.; Walcarius, A. Multi-Stimuli Photo and Redox Active Nanostructured Mesoporous Silica films on transparent electrodes. *ChemPhysChem* **2021**, *22*, 2464–2477. [[CrossRef](#)] [[PubMed](#)]
26. Alves, J.A., Jr.; Baldo, J.B. The Behavior of Zeta Potential of Silica Suspensions. *New J. Glass Ceram.* **2014**, *4*, 29–37.
27. Zhou, P.; Yao, L.; Chen, K.; Su, B. Silica Nanochannel Membranes for Electrochemical Analysis Molecular sieving: A Comprehensive Review. *Crit. Rev. Anal. Chem.* **2020**, *50*, 424. [[CrossRef](#)]
28. Basnig, D.; Vilà, N.; Herzog, G.; Walcarius, A. Voltammetric Behavior of Cationic Redox Probes at Mesoporous Silica film electrodes. *J. Electroanal. Chem.* **2020**, *872*, 113993. [[CrossRef](#)]
29. Etienne, M.; Goux, A.; Sibottier, E.; Walcarius, A. Oriented Mesoporous Organosilica Films on electrode: A New Class of Nanomaterials for Sensing. *J. Nanosci. Nanotechnol.* **2009**, *9*, 2398–2406. [[CrossRef](#)]
30. Vilà, N.; Ghanbaja, J.; Walcarius, A. Clickable Bifunctional and Vertically Aligned Mesoporous Silica Films. *Adv. Mater. Interfaces* **2016**, *3*, 1500440. [[CrossRef](#)]
31. Wilson, K.; Lee, A.F.; Macquarrie, D.J.; Clark, J.H. Structure and Reactivity of Sol-Gel Sulphonic Acid Silicas. *Appl. Catal. A* **2002**, *228*, 127–133. [[CrossRef](#)]
32. Shen, J.G.C.; Herman, R.G.; Klier, K. Sulfonic Acid-Functionalized Mesoporous Silica: Synthesis, characterization, and Catalytic Reaction of Alcohol Coupling to Ethers. *J. Phys. Chem. B* **2002**, *106*, 9975. [[CrossRef](#)]
33. Dijks, I.J.; van Ochten, H.L.F.; van Walree, C.A.; Geus, J.W.; Jennekens, L.W. Alkyl Sulphonic Acid Surface-Functionalized Silica as Heterogeneous Acid Catalyst in the Solvent Free Liquid-Phase Addition of Acetic Acid to Camphene. *J. Mol. Catal. A* **2002**, *188*, 209–224. [[CrossRef](#)]
34. Greczynski, G.; Hultman, L. X-Ray Photoelectron Spectroscopy: Towards reliable binding Energy Referencing. *Prog. Mater. Sci.* **2020**, *107*, 100590. [[CrossRef](#)]
35. Hanazaki, I.; Nagakura, S. Electronic Structure of the Tris(1,1'-dipyridyl)iron(II) Ion. *Inorg. Chem.* **1969**, *8*, 648–654. [[CrossRef](#)]
36. Alexander, B.D.; Dines, T.J.; Longhurst, R.W. DFT Calculations of the Structures and Vibrational Spectra of the [Fe(bpy)<sub>3</sub>]<sup>2+</sup> and [Ru(bpy)<sub>3</sub>]<sup>2+</sup> Complexes. *Chem. Phys.* **2008**, *352*, 19–27. [[CrossRef](#)]
37. Mallick, P.K.; Danzer, G.D.; Strommen, D.P.; Kincaid, J.R. Vibrational Spectra and Normal-Coordinate Analysis of Tris(bipyridine)ruthenium(II). *J. Phys. Chem.* **1988**, *92*, 5628–5634. [[CrossRef](#)]
38. Dines, T.J.; Peacock, R.D. Surface-Enhanced Resonance Raman Spectroscopy of Iron(II) and Ruthenium(II) Bipyridyl Complexes adsorbed on Silver Sols. *J. Chem. Soc. Faraday Trans.* **1988**, *84*, 3445–3457. [[CrossRef](#)]
39. Berger, R.M.; McMillin, D.R. Ultraviolet and Visible Resonance Raman spectroscopy of Tris-(2,2'-bipyridyl)iron(II): Intensity Considerations and Band Assignments. *Inorg. Chim. Acta* **1990**, *177*, 65–69. [[CrossRef](#)]
40. Caswell, D.S.; Spiro, T.G. Resonance Raman Spectra of the Ground and Charge-Transfer Excited State of Pentammine(4,4'-bipyridine)ruthenium(II) and Pentammine(4,4'-bipyridinium)ruthenium(II). *Inorg. Chem.* **1987**, *26*, 18–22. [[CrossRef](#)]
41. Tuchagues, J.P.; Bousseksou, A.; Molnar, G.; McGarvey, J.J.; Varret, F. The Role of Molecular Vibrations in the Spin Crossover Phenomenon. *Top. Curr. Chem.* **2004**, *235*, 85–103.
42. Bousseksou, A.; McGarvey, J.J.; Varret, F.; Real, J.A.; Tuchagues, J.-P.; Deniis, A.C.; Boillot, M.L. Raman Spectroscopy of the High- and Low-Spin States of the Spin Crossover complex Fe(phen)<sub>2</sub>(NCS)<sub>2</sub>: An Initial Approach to Estimation of vibrational contributions to the Associated Entropy Change. *Chem. Phys. Lett.* **2000**, *318*, 409–416. [[CrossRef](#)]
43. Takemoto, J.H.; Hutchinson, B. Low-Frequency Infrared Spectra of complexes which Exhibit Magnetic Crossover. I. Iron(II) complexes of 1,10-Phenanthroline and 2,2'-bipyridine. *Inorg. Chem.* **1973**, *12*, 705–708. [[CrossRef](#)]
44. König, E.; Madeja, K.; Watson, K.J. Reversible Quintet-Singlet Transition in Dithiocyanato-bis(2,2'-dipyridyl)iron(II). *J. Am. Chem. Soc.* **1968**, *90*, 1146–1153. [[CrossRef](#)]
45. van der Westhuizen, D.; von Eschwege, K.G.; Conradie, J. Electrochemistry and Spectroscopy of Substituted [Ru(phen)<sub>3</sub>]<sup>2+</sup> and [Ru(bpy)<sub>3</sub>]<sup>2+</sup> Complexes. *Electrochim. Acta* **2019**, *320*, 134540. [[CrossRef](#)]
46. Vilà, N.; Walcarius, A. Electrochemical Response of Vertically-aligned, Ferrocene-Functionalized Mesoporous Silica Films: Effect of the Supporting Electrolyte. *Electrochim. Acta* **2015**, *179*, 304–314. [[CrossRef](#)]
47. Chae, D.J.; Kim, D.Y.; Kim, T.G.; Sung, Y.M.; Kim, M.D. AlGaIn-based Ultraviolet Light-emitting Diodes using Fluorine-doped Indium Tin Oxide Electrodes. *Appl. Phys. Lett.* **2012**, *100*, 8–11.
48. Kober, E.M.; Meyer, T.J. Concerning the Absorption Spectra of the Ions M(bpy)<sub>3</sub><sup>2+</sup> (M = Fe, Ru, Os; bpy = 2,2'-bipyridine). *Inorg. Chem.* **1982**, *21*, 3967–3977. [[CrossRef](#)]

49. Decurtins, S.; Giidel, H.U.; Ludi, A.; Felix, F.; Ferguson, J. The Electronic spectrum of Tris(2,2'-bipyridine)ruthenium(II). *J. Am. Chem. Soc.* **1980**, *102*, 4096–4102.
50. Auböck, G.; Chergui, M. Sub-50-fs-Photoinduced Spin Crossover in  $[\text{Fe}(\text{bpy})_3]^{2+}$ . *Nat. Chem.* **2015**, *7*, 629–633. [[CrossRef](#)]
51. Azad, U.P.; Ganesan, V. Efficient Sensing of Nitrite by  $[\text{Fe}(\text{bpy})_3]^{2+}$  Immobilized Nafion Modified Electrodes. *Chem. Commun.* **2010**, *46*, 6156–6158. [[CrossRef](#)]
52. Vishnu, N.; Kumar, A.S. Development of Prussian blue and  $[\text{Fe}(\text{bpy})_3]^{2+}$  Hybrid Modified Pencil Graphite Electrodes Utilizing its Intrinsic Iron for electroanalytical Applications. *J. Electroanal. Chem.* **2017**, *786*, 145. [[CrossRef](#)]
53. De Graaf, C.; Sousa, C. Study of the Light-Induced Spin-Crossover Process of the  $[\text{Fe}(\text{bpy})_3]^{2+}$  Complex. *Chem. Eur. J.* **2010**, *16*, 4550–4556. [[CrossRef](#)] [[PubMed](#)]
54. Ahoulou, S.; Vilà, N.; Pillet, S.; Schaniel, D.; Walcarius, A. Coordination Polymers as Template for Mesoporous Silica Films: A Novel Composite Material  $\text{Fe}(\text{HTrz})_3@ \text{SiO}_2$  with Remarkable Electrochemical Properties. *Chem. Mater.* **2019**, *31*, 5796–5807. [[CrossRef](#)]
55. Ganesan, V.; Walcarius, A. surfactant templated sulfonic Acid Functionalized Silica Microspheres as New Efficient Ion Exchangers and Electrode Modifiers. *Langmuir* **2004**, *20*, 3632. [[CrossRef](#)]